Journal of Catalysis 269 (2010) 110–121

Contents lists available at ScienceDirect

Journal of Catalysis

journal homepage: www.elsevier.com/locate/jcat

Knoevenagel condensation reaction over acid–base bifunctional nanocrystalline $Ce_xZr_{1-x}O_2$ solid solutions

Georgeta Postole [a], Biswajit Chowdhury [b,*], Bikash Karmakar [c], Kumari Pinki [b], Julie Banerji [c], Aline Auroux [a,*]

[a] Institut de Recherches sur la Catalyse et l'Environnement de Lyon, UMR 5256, CNRS-UCB Lyon 1, 2 av. Albert Einstein, 69626 Villeurbanne Cedex, France
[b] Department of Applied Chemistry, Indian School of Mines University, Dhanbad 826 004, India
[c] Centre of Advanced Studies on Natural Products including Organic Synthesis, Department of Chemistry, University of Calcutta, 92, A.P.C. Road, Kolkata 700 009, India

ARTICLE INFO

Article history:
Received 3 June 2009
Revised 19 October 2009
Accepted 24 October 2009
Available online 1 December 2009

Keywords:
CeO_2
ZrO_2
Solid solution
Knoevenagel reaction
Acid–base bifunctional catalyst

ABSTRACT

Highly thermally stable three-dimensional spongelike mesoporous $Ce_xZr_{1-x}O_2$ solid solutions consisting of nanometer size particles with different Ce/Zr compositions were synthesized by a modified sol–gel procedure using a triethanolamine/water mixture as a solvent to be used in liquid Knoevenagel condensation reaction. These materials were investigated in detail by means of X-ray diffraction (XRD), Raman spectroscopy, chemical analysis, X-ray photoelectron spectroscopy (XPS), high-resolution transmission electron microscopy (HRTEM), UV–Vis spectroscopy, Fourier transform infrared spectroscopy (FT-IR) and adsorption microcalorimetry. The XRD, HRTEM and XPS studies proved the presence of nanocrystalline $Ce_xZr_{1-x}O_2$ solid solutions. These solid solutions showed excellent chemoselectivity in the classical Knoevenagel reaction. The large pore sizes (around 10 nm) highlight the possibility of using $Ce_xZr_{1-x}O_2$ as a support material for versatile catalytic systems. The results obtained from NH_3 and SO_2 adsorption microcalorimetry experiments successfully demonstrated the incorporation of ZrO_2 into the CeO_2 lattice resulting in both acidic and basic surface sites in a mixed oxide matrix.

1. Introduction

The synthesis and development of CeO_2 nanomaterials [1,2] with enhanced thermal, redox and acid–base properties are of paramount interest in designing and selecting catalysts for specific catalytic reactions [3]. The poor thermal stability of pure CeO_2 [4] is significantly improved in association with other elements such as Al, Si, La, Y, Hf and Gd in order to obtain solid solutions [5,6]. Recently, a new generation of mixed oxides containing CeO_2 and ZrO_2 with increased oxygen mobility, good thermal resistance and attractive catalytic applications has been developed [7,8]. The ceria–zirconia solid solutions present applications in heterogeneous catalysis, especially in SO_x removal, ethylbenzene dehydrogenation and water gas shift reactions [9]. It can also be noted that besides its redox properties, ceria–zirconia materials present remarkable acid–base properties which have not been investigated extensively. A thorough survey of the literature [10] suggests that oxygen mobility will be favoured in ceria–zirconia solid solutions because of the substitution of Ce^{4+} by the smaller Zr^{4+} cation. This phenomenon causes shrinkage of the CeO_2 fluorite-type lattice, which generates surface oxygen anions as basic sites in the catalyst. An alternative view is that, since CeO_2 and ZrO_2 have different lattice potentials, the incorporation of one oxide matrix into the other oxide matrix would cause a generation of surface acidity in the solid solution as per Kung's model [11]. Due to these acid–base properties, ceria–zirconia catalysts are also employed in fluid catalytic cracking, benzene combustion [12], cracking of tri isopropylbenzene [13], catalytic reduction of NO by CO [14] and in alcohol dehydration [15]. Nonetheless, the use of ceria–zirconia catalysts for fine chemical synthesis has not been studied extensively so far.

The classical Knoevenagel condensation reaction [16–18] is one of the most useful method for the synthesis of C=C bonds which could be applied to active dipolarophiles in 1,3-cycloaddition reactions. Knoevenagel condensation is actually a cross-aldol reaction between an aldehyde or ketone and an active methylene compound in the presence of an organic base such as pyridine, piperidine or ethylenediamine [16]. Malononitrile, cyanoesters, β-ketoesters, malonic acids and malonates are normally used as active methylene compounds containing two electron-withdrawing groups. Very recently attempts have been made to modify the reaction, avoiding organic bases to prevent unwanted by-products due to polymerization and self condensations. The use of different types of heterogeneous catalysts such as SBA-1 materials [19], amino-functionalized SBA-15 [20], solid bases [21] and solvents such as ionic liquids [22] has been reported. Therefore, the condensation reaction could be catalyzed not only by bases, but also by

* Corresponding authors. Fax: +91 326 2296615 (B. Chowdhury), +33 472 44 53 99 (A. Auroux).
E-mail addresses: biswajit_chem2003@yahoo.com (B. Chowdhury), aline.auroux@ircelyon.univ-lyon1.fr (A. Auroux).

0021-9517/$ - see front matter © 2009 Elsevier Inc. All rights reserved.
doi:10.1016/j.jcat.2009.10.022

acids or catalysts containing both acid–base sites. Recently, Bass et al. [23] and Katz and Davis [24] studied the synthesis of well-defined catalytic sites within silica via an imprinting method. Using the Knoevenagel condensation reaction, they evidenced acid–base cooperation between silanol and aminopropyl groups within single sites. Hruby and Shanks [25] also reported acid–base cooperation for the Knoevenagel reaction over functionalized silica surfaces. Therefore, developing a new solid catalyst possessing both acidic and basic properties is of utmost importance.

In this paper we report on the synthesis, characterization and catalytic activity of mesoporous ceria–zirconia nanocrystalline solid solutions with different Ce/Zr compositions (30/70, 50/50 and 70/30). As both pure ceria and zirconia are amphoteric, mesoporous ceria–zirconia mixed oxide catalysts have been synthesized in such a manner that both acidic and basic sites would be present concurrently on their surface. The $Ce_xZr_{1-x}O_2$ solid solutions have been characterized by XRD, Raman spectroscopy, ICP, BET surface area, pore distribution, XPS, HRTEM, FT-IR, UV–Vis, SO_2 and NH_3 adsorption microcalorimetry techniques which give a molecular level understanding of the mesoporous oxide surface. The catalytic performances of the synthesized samples were investigated in Knoevenagel condensation reaction, shedding light on the correlation between physicochemical properties and the activity of the ceria–zirconia mixed oxide catalyst.

2. Experimental

2.1. Catalyst synthesis

Three different Ce/Zr mixed oxides samples were synthesized in the present study: these are referred to hereafter as C/Z-30/70, C/Z-50/50 and C/Z-70/30, where the ratio XX/YY refers to the Ce/Zr molar ratio in the oxides. For simplicity, we denote it by C/Z throughout the text. Mesoporous ceria–zirconia catalysts have been prepared following a non-hydrothermal sol–gel approach. Cerium nitrate and zirconium oxychloride (Aldrich) were used as the precursors for cerium and zirconium, respectively. Triethanolamine (Acros) was used as the structure-directing template.

In the typical procedure, $Ce(NO_3)_2$ (0.003 mole) was added to 0.02 mole of triethanolamine under stirring at room temperature, followed by the addition of $ZrOCl_2$ (0.007 mole) to the mixture. Subsequently, 0.01 mole of tetraethylammonium hydroxide (E-Merck, Germany) was added dropwise to the solution. Finally, 0.11 mole of water was added and the solution was aged for 24 h and dried at 110 °C for 24 h. The sample was then calcined at 700 °C for 10 h with a temperature rise of 1 °C/min.

2.2. Characterization

2.2.1. X-ray diffraction

X-ray diffraction spectra were recorded using a Bruker (Siemens) D5005 diffractometer (Ni-filtered Cu Kα radiation, $\lambda = 1.5406$ Å). The crystallite sizes were calculated from recorded XRD pattern using a whole-powder pattern fitting method (the Rietveld refinement) [26]. The structural characteristics of ceria–zirconia samples were calculated from Lamas et al. [27].

2.2.2. Raman spectroscopy

Raman scattering experiments were performed in the back-scattering configuration from 200 to 1000 cm^{-1} at room temperature for each sample in the powder form. The 514 nm line of the Ar-ion laser was used, which was focused to a spot size of ~2 μm with an incident laser power of ~1 mW. Raman spectra were recorded in a LabRAM HR Jobin–Yvon spectrograph coupled to a microscope. The spectral resolution was 3 cm^{-1} and the spectra acquisition consisted of five accumulations of 15 s for each sample.

2.2.3. ICP-AES analysis

The chemical compositions (metal contents) were determined by AES-ICP in a Spectroflame-ICP instrument, after the samples were dissolved using a mixture of inorganic acids (H_2SO_4, HNO_3 and HF).

2.2.4. BET surface area and pore distribution

The characterization of the porous texture of the prepared materials and the determination of the specific surface area were carried out by physical adsorption of N_2 at −196 °C using a Micromeritics ASAP 2020 apparatus. Prior to the analysis, the samples were outgassed at 400 °C for 4 h. The adsorption data were analyzed using the ASAP 2020 software based on the Brunauer–Emmett–Teller (BET) isotherm and the Barret Joyner Halenda (BJH) method. The BET equation was used to calculate the apparent surface area from the data obtained at P/P_0 between 0.05 and 0.25. The cross-sectional area of the nitrogen molecule was assumed to be 16.2 Å. The BJH method takes into account the capillary condensation using the Kelvin equation and it is useful for the determination of the pore size distribution for mesopores. The eventual microporosity was calculated by applying the *t*-plot method. In this work, according to IUPAC nomenclature, the micropores have been defined as $d < 2$ nm; mesopores $d = 2$–50 nm and macropores $d > 50$ nm. From the pore size distribution, a cumulative pore volume can be calculated. The technique employed for adsorption data analysis was valid exclusively for the micro- and mesopore ranges.

2.2.5. X-ray photoelectron spectra

The X-ray photoelectron spectra were recorded on an Axis Ultra Dld spectrometer from Kratos Analytical with a monochromatic Al Kα X-ray source (150 W). Widescans were taken at pass energy of 100 eV and scans of photopeaks were taken at pass energy of 40 eV. The contaminant C1s signal was chosen as a reference, with a binding energy of 284.6 eV. The XPS analysis was performed at ambient temperature and at pressure typically of the order of $<10^{-9}$ Pa.

2.2.6. HRTEM analysis

TEM images were obtained from a Hitachi H-9000 NAR transmission electron microscope at an operating voltage of 100 kV. The sample was prepared by placing one drop of dispersed solution of the catalyst in acetone solvent on a carbon-coated copper grid followed by drying in air.

2.2.7. DR UV–Vis spectroscopy

Diffuse reflectance UV–Vis spectra in the 1100–200 nm range were obtained with a Perkin–Elmer Lambda 35 spectrophotometer, operating at room temperature. The Kubelka–Munk function ($F(R\infty)$) was used to convert diffuse reflectance data into absorption spectra using spectralon as a standard.

2.2.8. FT-IR spectroscopy

FT-IR spectra were recorded on a Vector 22 spectrometer from Bruker with a resolution of 2 cm^{-1}, using the KBr dilution technique for the analysis of the mixed cerium–zirconium oxides. The spectra (50 scans) were recorded in the 400–4000 cm^{-1} wavenumber range.

2.2.9. Adsorption microcalorimetry

The adsorption experiments were performed at 80 °C in a heat-flow microcalorimeter (Tian-Calvet type, C80 from Setaram) linked to a conventional volumetric apparatus and equipped with a Barocel capacitance manometer (Datametrics) for pressure

measurements. The catalysts, fresh samples (around 0.100 g), were pretreated overnight under air at 400 °C. Prior to the NH_3/SO_2 adsorption, the catalysts were outgasssed also at 400 °C for 1 h. The differential heats of adsorption were measured as a function of coverage by repeatedly sending small doses of NH_3/SO_2 over the catalysts until an equilibrium pressure of about 67 Pa was reached [28]. The sample was then outgassed for 30 min at the same temperature and a second adsorption was performed (still at 80 °C) until an equilibrium pressure of about 27 Pa was attained in order to calculate the amount of irreversible adsorption at this pressure. The difference between the amounts of gas adsorbed at 27 Pa during the two adsorption runs corresponded to the number of strong adsorption sites.

2.3. General procedure for the Knoevenagel reaction

The aldehyde (0.5 g, 1.0 equiv.) and active methylene compound (0.35 g, 1.1 equiv.) were placed in a 50 mL round-bottomed flask, and then 5 mL of ethanol (95%) was added. The mixture was stirred with a magnetic stirrer at 600 rpm speed at room temperature till a homogeneous solution was obtained. Then 0.010 g catalyst (C/Z) (previously ground and sieved to obtain particles of 0.1–0.2 mm diameter) was added and stirring was continued under reflux conditions at 80 °C in air atmosphere.

In this work, the speed of the stirrer was chosen to ensure that the reaction rate was free from external diffusion influence. To check this point, catalytic tests were performed at different speeds of stirring in the range of 100–800 rpm. It was observed that for speeds higher than 400 rpm the rate of the reaction remained constant and the external diffusion is not a rate-controlling step. Moreover, previous to the reported test, different quantities of sample were also used to ensure that the reaction rate was free from extragranular diffusion. Also, the dimensionless quantity Φ, $\Phi = (\frac{dN}{dt}\frac{1}{c_0}\frac{R^2}{D})$ [29], containing only observable quantities (reaction rate, reactant concentration, particle size and diffusivity) was found to be 0.21 thus confirming the absence of intragranular diffusion in the present case.

The extent of consumption of the reactants was monitored by thin layer chromatography (TLC) [30]. After completion of the reaction (i.e. one of the starting materials has totally disappeared as monitored by TLC method), the mixture was filtered and the residue was dried and reused as a catalyst. The filtrate was dried under vacuum and adsorbed on 60–120 mesh silica gel (Merck) and the crude was purified by column chromatography using 60–120 silica gel and 6–10% ethyl acetate/petroleum ether as an eluent. The purified products were characterized by ^{1}H NMR, ^{13}C NMR and FT-IR spectroscopy.

The reusability of the C/Z-30/70 catalyst was carried out with benzaldehyde and malononitrile as substrates in ethanol medium at 80 °C by adopting the following protocol under similar experimental conditions as described above. After the completion of the reaction, the catalyst was filtered and dried. Fresh quantities of benzaldehyde (1.0 mmol) and malononitrile (1.1 mmol) were used and the C/Z-30/70 catalyst was thus reused for three cycles adopting the identical protocol.

2.4. Spectral data of some selected compounds

The ^{1}H NMR (300 MHz) and ^{13}C NMR (75.5 MHz) spectra were done on a Bruker-AVANCE Digital MHz NMR spectrometer. TMS was used as an internal standard and chemical shift values were in δ (ppm). FT-IR spectra were obtained using a Perkin–Elmer RX-1 spectrophotometer and done on KBr disc.

(a) Benzylidene malononitrile (**2a**): Pale yellow crystalline solid, ^{1}H NMR (300 MHz, $CDCl_3$): δ (ppm) = 7.79 (s, 1H, alkenic), 7.90 (d, 2H, aromatic, J = 7.2 Hz), 7.67–7.61 (m, 2H, aromatic), 7.58–7.27 (m, 1H, aromatic); ^{13}C NMR (75.5 MHz, $CDCl_3$): δ (ppm) = 130.9 (C), 113.7 (C), 112.5 (C), 82.9 (C), 134.6 (CH), 130.7 (CH), 129.6 (CH), 159.9 (CH); IR (KBr): 3431, 2981, 2222, 1723, 1604, 1257, 1200, 1088 cm^{-1}.

(b) Benzylidene ethylcyanoacetate (**2b**): Pale yellow crystalline solid, ^{1}H NMR (300 MHz, $CDCl_3$): δ (ppm) = 8.25 (s, 1H, alkenic), 8.0 (d, 2H, aromatic, J = 6.8 Hz), 7.47–7.59 (m, 3H, aromatic), 4.39 (q, 2H, aliphatic, J = 7.1 Hz), 1.40 (t, 3H, aliphatic, J = 7.1 Hz); ^{13}C NMR (75.5 MHz, $CDCl_3$): δ (ppm) = 162.5 (C), 131.5 (C), 115.4 (C), 103.0 (C), 155.0 (CH), 133.3 (CH), 131.0 (CH), 129.2 (CH), 62.7 (CH_2), 14.1 (CH_3); IR (KBr): 3437, 2933, 2221, 1655, 1586, 1448, 1215, 958 cm^{-1}.

(c) 4-Nitrobenzylidene malononitrile (**2c**): Yellow crystalline solid, ^{1}H NMR (300 MHz, $CDCl_3$): δ (ppm) = 7.81 (s, 1H, alkenic), 8.01 (d, 2H, aromatic, J = 9.3 Hz), 8.33 (d, 2H, aromatic, J = 8.7 Hz); ^{13}C NMR (75.5 MHz, $CDCl_3$): δ (ppm) = 135.8 (C), 112.6 (C), 111.6 (C), 87.6 (C), 150.4 (C), 156.8 (CH), 131.3 (CH), 124.6 (CH); IR (KBr): 3437, 2928, 2223, 1580, 1522, 1346, 935 cm^{-1}.

(d) 4-Nitrobenzylidene ethylcyanoacetate (**2d**): Pale yellow crystalline solid, ^{1}H NMR (300 MHz, $CDCl_3$): δ (ppm) = 8.30 (s, 1H, alkenic), 8.13 (d, 2H, aromatic, J = 9.0 Hz), 8.35 (d, 2H, aromatic, J = 8.7 Hz), 4.43 (q, 2H, aliphatic, J = 7.2 Hz), 1.42 (t, 3H, aliphatic, J = 7.2 Hz); ^{13}C NMR (75.5 MHz, $CDCl_3$): δ (ppm) = 162.1 (C), 137.0 (C), 112.2 (C), 86.1 (C), 149.3 (C), 151.7 (CH), 124.3 (CH), 131.5 (CH), 63.4 (CH_2), 14.1 (CH_3); IR (KBr): 3421, 2933, 2364, 1773, 1607, 1517, 1348, 1270, 1201, 856 cm^{-1}.

(e) 4-Methylbenzylidene malononitrile (**2e**): White crystalline solid, ^{1}H NMR (300 MHz, $CDCl_3$): δ (ppm) = 7.72 (s, 1H, alkenic), 7.81 (d, 2H, aromatic, J = 8.1 Hz), 7.34 (d, 2H, aromatic, J = 8.1 Hz), 2.46 (s, 3H, tolyl); ^{13}C NMR (75.5 MHz, $CDCl_3$): δ (ppm) = 128.5 (C), 114.0 (C), 112.8 (C), 81.2 (C), 146.4 (C), 159.7 (CH), 130.9 (CH), 130.4 (CH), 22.0 (CH_3); IR (KBr): 3436, 2929, 2220, 1586, 1413, 1184, 1036, 815 cm^{-1}.

(f) 4-Chlorobenzylidene malononitrile (**2g**): White crystalline solid, ^{1}H NMR (300 MHz, $CDCl_3$): δ (ppm) = 7.73 (s, 1H, alkenic), 7.85 (d, 2H, aromatic, J = 8.6 Hz), 7.53 (d, 2H, aromatic, J = 8.7 Hz); ^{13}C NMR (75.5 MHz, $CDCl_3$): δ (ppm) = 129.3 (C), 113.4 (C), 112.3 (C), 83.4 (C), 141.2 (C), 158.2 (CH), 131.8 (CH), 130.1 (CH); IR (KBr): 3438, 2926, 2223, 1579, 1407, 1288, 1090, 1006, 824 cm^{-1}.

(g) 4-Chlorobenzylidene ethylcyanoacetate (**2h**): White crystalline solid, ^{1}H NMR (300 MHz, $CDCl_3$): δ (ppm) = 8.2 (s, 1H, alkenic), 7.93 (d, 2H, aromatic, J = 2.7 Hz), 7.48 (d, 2H, aromatic, J = 2.7 Hz), 4.39 (q, 2H, aliphatic, J = 7.0 Hz), 1.4 (t, 3H, aliphatic, J = 7.2 Hz); ^{13}C NMR (75.5 MHz, $CDCl_3$): δ (ppm) = 162.2 (C), 129.9 (C), 115.2 (C), 103.5 (C), 139.6 (C), 153.4 (CH), 129.7 (CH), 132.2 (CH), 62.8 (CH_2), 14.1 (CH_3); IR (KBr): 3443, 2925, 2369, 1686, 1589, 1422, 1291, 1087, 931 cm^{-1}.

(h) 3-Nitrobenzylidene ethylcyanoacetate (**2j**): Pale yellow crystalline solid, ^{1}H NMR (300 MHz, $CDCl_3$): δ (ppm) = 8.70 (s, 1H, alkenic), 7.74 (t, 1H, aromatic, J = 8.1 Hz), 8.31 (s, 1H, aromatic), 8.40–8.43 (m, 1H, aromatic), 8.40–8.43 (m, 1H, aromatic), 4.42 (q, 2H, aliphatic, J = 7.1 Hz), 1.42 (t, 3H, aliphatic, J = 7.2 Hz); ^{13}C NMR (75.5 MHz, $CDCl_3$): δ (ppm) = 161.5 (C), 132.9 (C), 114.5 (C), 106.7 (C), 148.6 (C), 151.8 (CH), 135.1 (CH), 130.5 (CH), 127.1 (CH), 125.9 (CH), 63.3 (CH_2), 14.1 (CH_3); IR (KBr): 3437, 2927, 2376, 1721, 1610, 1529, 1469, 1353, 1215, 768 cm^{-1}.

(i) Furfurylidene malononitrile (**2k**): White crystalline solid, ^{1}H NMR (300 MHz, $CDCl_3$): δ (ppm) = 7.52 (s, 1H, alkenic), 7.36 (d, 1H, aromatic, J = 3.7 Hz), 7.81 (d, 1H, aromatic, J = 1.6 Hz), 6.72 (q, 1H, aromatic, J = 2.2); ^{13}C NMR (75.5 MHz, $CDCl_3$): δ (ppm) = 148.1 (C), 113.8 (C), 112.6 (C), 123.4 (CH), 114.5 (CH), 143.1 (CH), 149.6 (CH); IR (KBr): 3437, 3017, 2220, 1681, 1602, 1415, 1218, 1062, 768 cm^{-1}.

3. Results and discussion

3.1. Catalyst characterization

3.1.1. X-ray diffraction and Raman spectroscopy

The XRD spectra of the Ce/Zr mixed oxides are presented in Fig. 1. The diffraction patterns demonstrated the formation of a single solid solution-like ceria–zirconia phase ($Ce_xZr_{1-x}O_2$), as peak splitting for the presence of two phases could not be detected. It is known that the crystal structures of CeO_2–ZrO_2 solid solutions and their structural parameters strongly depend on the synthesis method. As the cerium content varies, ceria–zirconia solid solutions exhibit a cubic–tetragonal structural phase transition where the ideal fluorite-type structure has the space group *Fm*-3*m* and the tetragonal phase belongs to the $P4_2/nmc$ group and has oxygen displacements from an ideal fluorite position. Colon et al. [31] showed that $Ce_xZr_{1-x}O_2$ solid solutions exhibit a fluorite-type cubic structure for $x > 0.5$ and a tetragonal one for $x \leqslant 0.5$. However, the metastable tetragonal phase has been reported to be easily formed in a wide interval of compositions, for example when the ceramic method is employed for the synthesis of ceria–zirconia solid solution [32]. The different structures of CeO_2–ZrO_2 materials seem to be strongly influenced by the cooling conditions, as noticed and discussed by several authors [32]. As it can be seen in Fig. 1, the three C/Z samples displayed broad peaks and due to their low crystallinity it was not possible to establish clearly from the X-ray results whether the solid solutions presented tetragonal or cubic structures. The most intense lines were shifted to higher diffraction angles with increasing ZrO_2 content. This observation was attributed to shrinkage of lattices due to the replacement of Ce^{4+} (ionic radius 0.098 nm) with a smaller Zr^{4+} (ionic radius 0.084 nm) in agreement with the Vegard rule [33]. Using the Rietveld method, which involves a global analysis of the whole XRD pattern, Lamas et al. [27] found that powders with CeO_2 content up to 70 mol% exhibit a tetragonal structure ($P4_2/nmc$ space group). Those authors observed in the case of a 70 mol% CeO_2 sample a large oxygen displacement, confirming the presence of tetragonal phase for this concentration. For a solid solution containing 80 mol% CeO_2, the $P4_2/nmc$ and *Fm*-3*m* structural models gave similar agreement factors, while a sample with 90 mol% CeO_2 presented a cubic structure. Consequently, in order to determine the lattice parameters and the corresponding crystallite sizes, Rietveld refinements were performed by assuming the $P4_2/nm$ space group for the tetragonal phase, with (Zr^{4+}, Ce^{4+}) cations and O^{2-} anions in 2*a* and 4*d* positions, respectively. The calculated crystallite sizes were in the 7–10 nm range, and the obtained structural characteristics of ceria–zirconia samples are reported in Table 1. The increase of Zr^{4+} amount induced a smaller cell volume in the case of $Ce_xZr_{1-x}O_2$ solid solution. The cell parameters (*a* and *c*) for the C/Z samples calculated from the main diffraction peaks displayed a linear decrease with increasing ZrO_2 content. It has to be pointed out that similar Rietveld refinements were not performed by opening the fitting to cubic phase, and that most probably the true nature of ceria–zirconia solid solutions is a mixture of the two phases: cubic and tetragonal. For instance, the peak at 29° observed for C/Z-70/30 seems to contain contributions of the cubic (1 1 1) and tetragonal (1 1 1) planes, while the catalyst C/Z-30/70 mainly presents tetragonal structure, as deduced from the position of the main peak at around 30°, which is that expected for the tetragonal (1 1 1) plane. The use of Rietveld refinements by assuming the tetragonal phase did not induce important errors in the obtained results, as observations by electron microscopy of the samples have revealed that the mean particle size is in good agreement with the XRD determination. Moreover, the concentration of Ce was also estimated, and approximate compositions of $Ce_{0.37}Zr_{0.63}O_2$, $Ce_{0.61}Zr_{0.39}O_2$ and $Ce_{0.76}Zr_{0.24}O_2$ were obtained for C/Z-30/70, C/Z-50/50 and C/Z-70/30, respectively, similar to those observed by using ICP and XPS analysis (see Table 2 and Section 3.1.4).

Raman spectroscopy was also used to further elucidate the structure of the CeO_2–ZrO_2 mixed oxides. According to the literature, six Raman-active modes ($A_{1g} + 2B_{1g} + 3E_g$, space group $P4_2/nmc$) of symmetry centred at 147, 268, 313, 460, 600 and 645 cm^{-1} can be observed for *t*-ZrO_2, while for cubic CeO_2, only one F_{2g} mode centred at around 465 cm^{-1} is Raman-active [34]. In the obtained Raman spectra (not shown here), for catalyst C/Z-70/30 the F_{2g} peak appeared at 467 cm^{-1} and other two weak bands were observed at around 300 and 620 cm^{-1}, respectively, assigned to a tetragonal phase. By contrast, the strongest bands for C/Z-50/50 and C/Z-30/70 were considerably less intense and appeared at lower frequencies: 460 and 452 cm^{-1}, respectively. The bands for the tetragonal phase increased in intensity with increasing ZrO_2 content.

A comparison of the data obtained from XRD and Raman shows that the tetragonal phase is predominant in C/Z-30/70 and C/Z-50/50, while on C/Z-70/30 cubic and metastable tetragonal phases coexist.

3.1.2. ICP-AES analysis

The results obtained from the elemental ICP-AES analysis are presented in Table 2. As expected, the cerium content increased

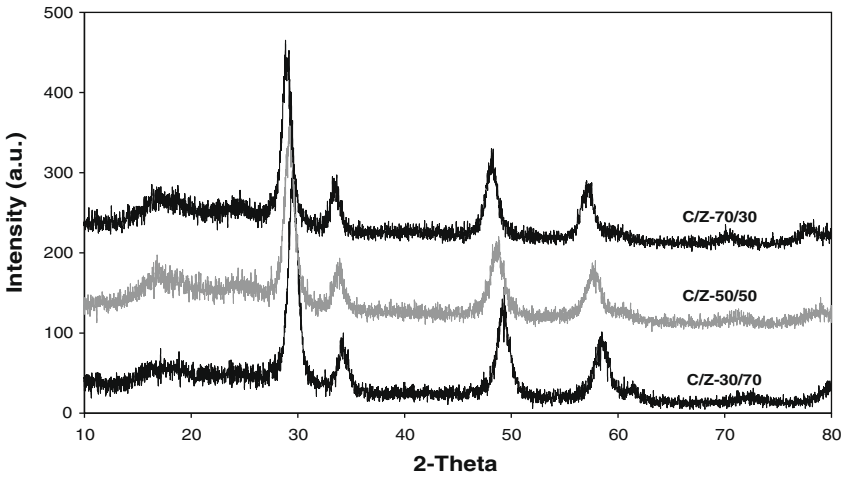

Fig. 1. X-ray diffraction patterns for C/Z samples.

Table 1
Structural characteristics of C/Z samples.

Sample	Lattice	Cell dimension			Crystallite size (nm)
		$a = b$ (Å)	c (Å)	V (Å^3)	
C/Z-30/70	T	3.69	5.25	71.63	7.6
C/Z-50/50	T	3.75	5.31	74.56	8.2
C/Z-70/30	T	3.78	5.35	76.5	7.6

Table 2
ICP-AES data for C/Z samples.

Sample	ICP-AES		
	$Ce_xZr_{1-x}O_2$	Ce (wt.%)	Zr (wt.%)
C/Z-30/70	$Ce_{0.44}Zr_{0.56}O_2$	32.24	40.50
C/Z-50/50	$Ce_{0.62}Zr_{0.38}O_2$	46.27	28.23
C/Z-70/30	$Ce_{0.77}Zr_{0.23}O_2$	58.13	17.07

in the order Ce/Zr = 30/70 < 50/50 < 70/30 and the zirconia content decreased in the same order.

3.1.3. BET surface area and pore characteristics

The textural features of the samples have been investigated by BET surface area measurements and the results are reported in Table 3. The specific surface areas of the C/Z samples range from ca. 30 to 50 m^2/g. The high surface area, even after calcination at 700 °C, remained in the same range as reported in the literature [35]. Among the samples tested, it can be noted from Table 3 that the lowest surface area was obtained for sample C/Z-50/50, with the largest particle sizes as determined by XRD and textural analysis (Table 1). The lack of a clear trend of BET surface areas with the zirconium content could be attributed to the fact that each composition presents a different crystalline structure or even a mixture of crystalline structures. A similar dependence of the BET surface area on the zirconium loading was reported by Adamowska et al. [36] for a set of commercial $Ce_xZr_{1-x}O_2$ samples. The argument provided to explain such a trend was that crystal growth may occur upon the insertion of ZrO_2 in the CeO_2 lattice for zirconia contents smaller than or equal to 50 mol%, inducing a decrease in the solid solution surface area. For zirconia contents higher than 50 mol%, ZrO_2 was found to be responsible for a progressive change in the solid solution structure, resulting in an increase of its surface area.

The adsorption/desorption isotherms and the corresponding pore size distributions of the studied catalysts are reported in Fig. 2. Type IV isotherms can be observed in all cases, characterized by the presence of a hysteresis loop indicating that the C/Z samples are mesoporous in nature. Indeed, the micropore analysis of the C/Z catalysts using DeBoer's t-plot confirmed the absence of significant microporosity (V_{micro} < 2% of V_t). By applying the BJH (Barrett, Joyner and Halenda) method to the desorption branch of the isotherm, the pore size distributions for C/Z samples have been obtained (see the inset of Fig. 2). The catalysts present quite a narrow distribution of pore diameter located between 4 and 20 nm. The average pore diameter decreased from C/Z-50/50 to C/Z-30/70 and C/Z-70/30.

3.1.4. X-ray photoelectron spectra

XPS experiments were carried out in order to ascertain the chemical nature and type of elements present on the surface of ceria–zirconia mixed oxide, and are presented in Fig. 3. In the XPS elemental survey spectra of the studied samples, the presence of carbon (5.67, 5.81 and 7.12 at.% for C/Z-30/70, C/Z-50/50 and C/Z-70/30, respectively), oxygen, zirconium, cerium (see Table 4) and Na (3.67, 2.99 and 2.69 at.% for C/Z-30/70, C/Z-50/50 and C/Z-70/30, respectively) could be confirmed. The spectra of the

Table 3
BET and textural data for C/Z samples.

Sample	S_{BET} (m^2/g)	S_{BJH} (m^2/g)	S_{micro} (m^2/g)	Cumulative pore volume (cm^3/g)	Average pore diameter (nm)
C/Z-30/70	49.9	67.1	1.5	0.15	8.9
C/Z-50/50	33.8	39.7	1.0	0.10	10.3
C/Z-70/30	40.4	50.9	0	0.09	7.3

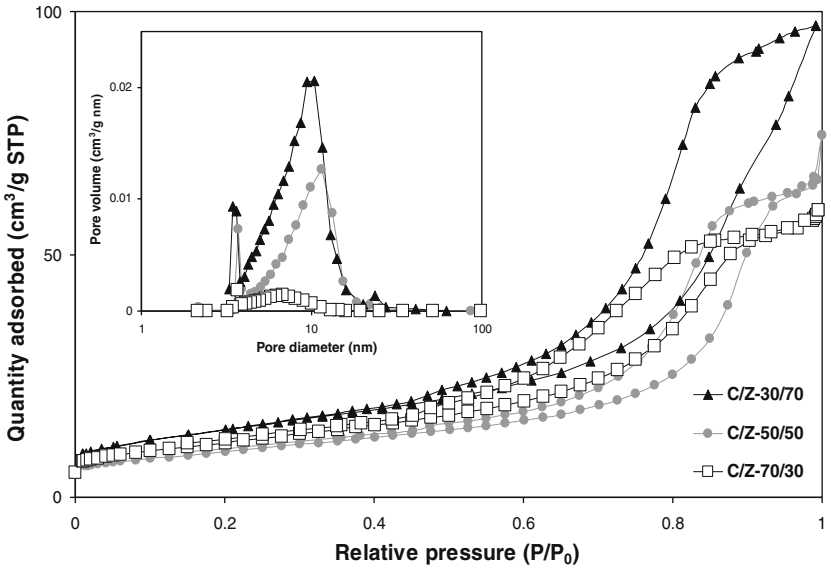

Fig. 2. Adsorption/desorption isotherms and pore size distribution for C/Z catalysts.

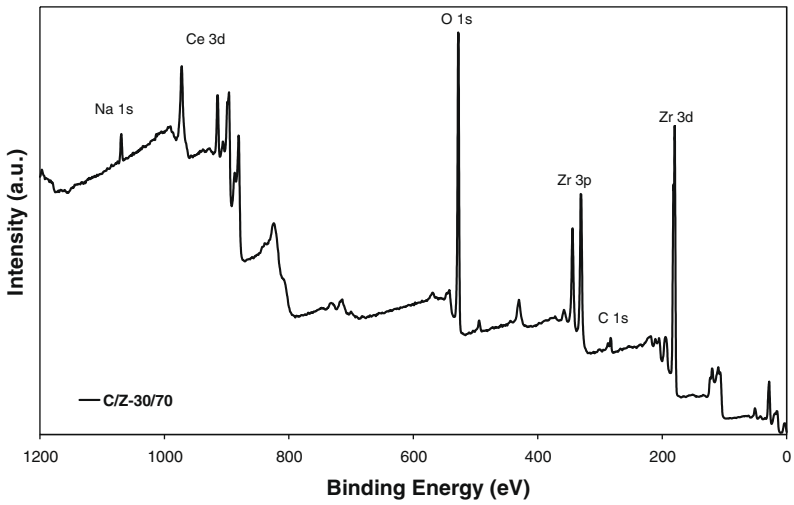

Fig. 3. XPS survey spectrum of C/Z-30/70 catalyst.

Table 4
XPS data for C/Z samples.

Sample	Ce $3d_{5/2}$		Zr $3d_{5/2}$		O 1s		Ce/Zr at. ratio	O/(Ce + Zr) at. ratio
	at.%	BE (eV)	at.%	BE (eV)	at.%	BE (eV)		
C/Z-30/70	13.1	882.1	16.3	181.7	61.2	529.4	0.80	2.08
C/Z-50/50	19.4	882.3	12.1	181.9	59.7	529.5	1.60	1.89
C/Z-70/30	23.7	882.0	8.3	181.9	58.2	529.3	2.87	1.82

other samples were quite similar and therefore not shown here. The nature of interactions in the samples of CeO_2–ZrO_2 with different molar ratios has also been investigated by XPS technique. The electron-binding energies (BE (eV)) of the photoelectron peaks pertaining to O 1s, Zr 3d and Ce 3d together with the corresponding atomic ratios are shown in Table 4.

As depicted in Fig. 4A, the X-ray photoelectron spectra of ceria are rather complex because of the hybridization between the outer 4f levels and the O 2p state. The main band of Ce $3d_{5/2}$ at 882.1 eV which corresponds to Ce^{4+} was observed for all samples. The Ce $3d_{5/2}$ and Ce $3d_{3/2}$ levels each presents five components, labelled V_0, V, V′, V″ and V‴ and U_0, U, U′, U″ and U‴, respectively. According to the literature [37], the Ce 3d spectra can be assigned as follows: the peaks labelled U are due to $3d_{3/2}$ spin–orbit states, and those labelled V are due to the corresponding $3d_{5/2}$ states. The U‴/V‴ doublet is due to the primary photoemission from Ce(IV)O_2, i.e. Ce $3d^9$ $4f^0$ O $2p^6$ Ce(IV) .The U/V and U″/V″ doublets are shake-down features resulting from the transfer of one or two electrons from a filled O 2p orbital to an empty Ce 4f orbital, i.e. Ce $3d^9$ $4f^2$ O $2p^4$ and Ce $3d^9$ $4f^1$ O $2p^5$ Ce(IV) in the final states. The U′/V′ doublet is due to photoemission from Ce cations, i.e. Ce $3d^9$ $4f^1$ O $2p^6$ of Ce (III). The cerium is mainly present in the Ce^{4+} oxidation state (more than 90 at.%). There is a decrease in the values of BE of Ce $3d_{5/2}$ component (882.1 eV) compared to that for bulk CeO_2 (882.9 eV). This shift can be interpreted in terms of the interaction between zirconia and cerium oxide species, i.e. Ce–O–Zr bond formation.

As shown in Fig. 4B, the O 1s peak is, in general, broad and complicated because of the non-equivalence of surface oxygen ions. As reported in the literature [38], the oxygen ions in pure CeO_2 exhibit intense peaks at 528, 528.8, 529.0 and 530.1 eV while the oxygen ions in pure ZrO_2 show an intense peak at 530.6 eV. The observation of the peak shape in Fig. 4B suggests that the O 1s spectrum is composed of more than one peak arising from the overlapping contributions of oxygen from ceria, zirconia and Ce–Zr–O compounds. The two peaks observed at 529.4 and 531.7 eV (see the insert of Fig. 4B) have been ascribed to oxide ions (lattice oxygen) and surface hydroxyl groups, respectively.

The Zr 3d photoemission spectra (Fig. 4C) of the samples exhibit a doublet corresponding to Zr $3d_{3/2}$ around 184.1 eV and Zr $3d_{5/2}$ around 181.7 eV. Interestingly the binding energy of Zr $3d_{5/2}$ is higher than that in Zr metal (180.0 eV), lower than that in ZrO_2 (182.9 eV), but similar to that in ZrO_x ($0 < x < 2$, 181.4 eV) [39]. Therefore, the XPS study also proves the formation of $Ce_xZr_{1-x}O_2$ solid solutions.

Using the values of the surface atomic composition as shown in Table 4, the Ce/Zr and O/(Ce+Zr) atomic ratio can be estimated for the depth probed by XPS, which yields $Ce_{0.44}Zr_{0.56}O_{2.08}$, $Ce_{0.62}Zr_{0.38}O_{1.89}$ and $Ce_{0.74}Zr_{0.26}O_{1.82}$ for samples C/Z-30/70, C/Z-50/50 and C/Z-70/30, respectively. It is interesting to note that the amount of surface oxygen in the solid solution increased upon increasing the zirconia content. The possibility of the presence of Ce^{3+} which favours the formation of oxygen vacancies in the mixed oxide surface [40] cannot be ignored. It can be speculated that a chemical pumping effect causes oxygen to diffuse up to the surface, reaching the vacant sites. As discussed in the literature [41], the reduction of ceria is presumably controlled by the nature of the oxygen vacancies, since oxygen diffusion, the rate-controlling step, depends on the type, size and concentration of oxygen vacancies.

3.1.5. HRTEM study

The HRTEM pictures (Fig. 5) show highly dispersed nanoparticles of cerium and zirconium. Due to the similarities of the micrographs obtained for the three studied samples, only the micrographs corresponding to C/Z-30/70 catalyst are presented. These show a particle size in the 7–10 nm range, which is in agreement with the XRD data. The images show a spongelike structure where two different types of nanoparticles are observed. The presence of mesopores in the mixed oxide matrix is apparent, thereby

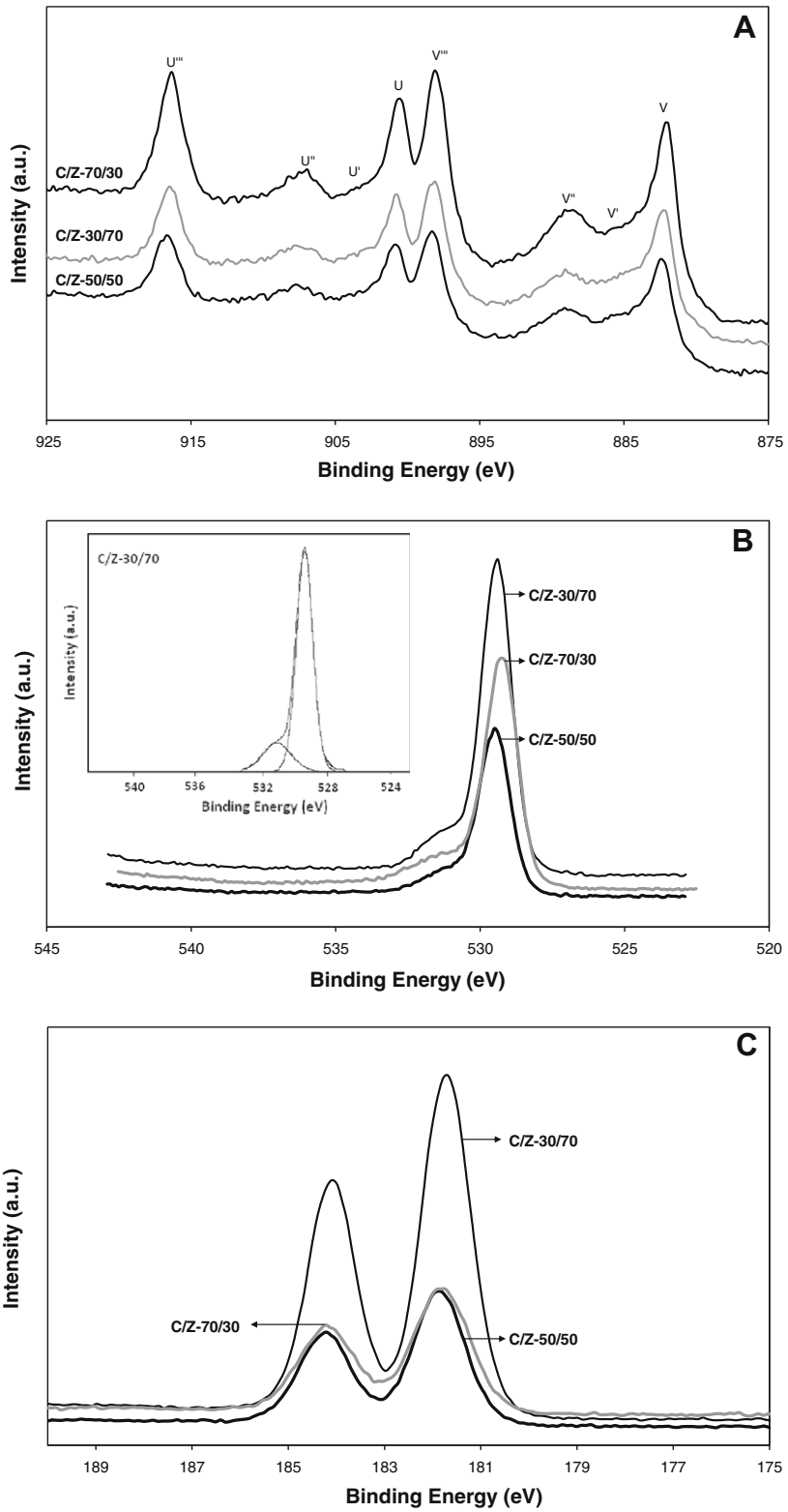

Fig. 4. (A) XPS of the Ce $3d_{5/2}$ region for Ce–Zr mixed oxides; (B) XPS O 2p spectra of C/Z samples and the deconvoluted spectra for C/Z-30/70 sample (in inset); (C) XPS of the Zr $3d_{5/2}$ region for ceria–zirconia mixed oxides.

corroborating the pore size measurement data. As reported by Liang et al. [40], colloidal ceria clusters have been exploited as both physical and chemical templates to generate ceria–zirconia nanocomposites with narrow size distribution via modified Kirkendall effect.

3.1.6. Diffuse reflectance UV–Vis spectra

A comparison of the electronic spectra of the mixed ceria–zirconia oxides with different molar ratios is made in Fig. 6. As can be seen from the figure, the ceria–zirconia solid solutions give rise to absorption bands near 350, 246 and 210 nm (3.54, 5.04 and

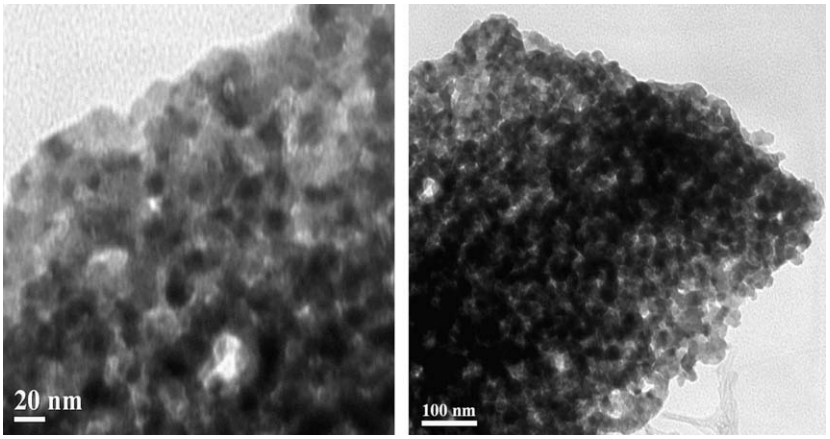

Fig. 5. HRTEM images of the C/Z-30/70 catalyst.

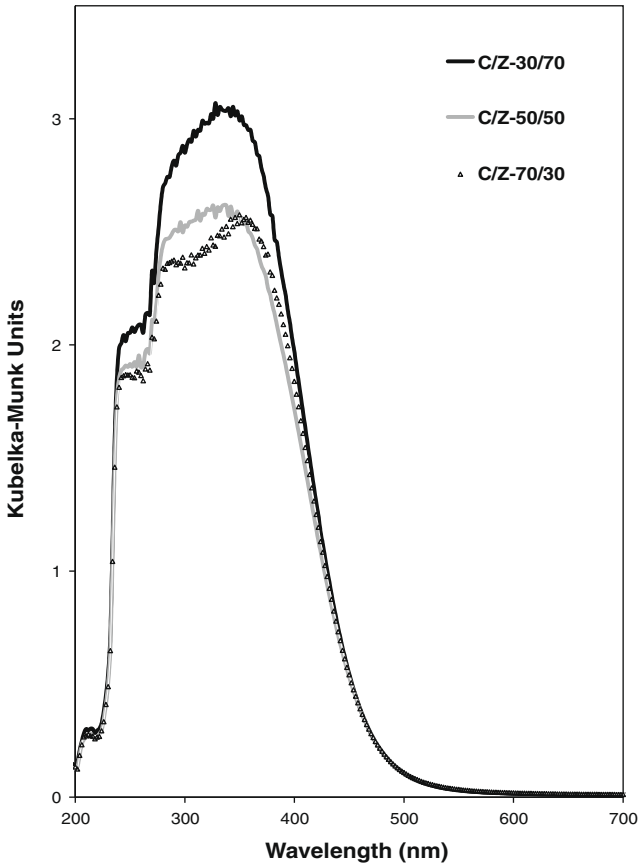

Fig. 6. UV–Vis diffuse reflectance spectra of C/Z-30/70, C/Z-50/50 and C/Z-70/30 samples.

5.9 eV, respectively). It is interesting to note that for the higher CeO_2 contents, the peak components become distinguishable. The mixed oxide with ceria concentration of 70% (C/Z-70/30) displays two clear components whereas in the others only a broad absorption edge is observed. At loading of 70% ceria, a band appears more clearly at 284 nm. Ceria is an n type semiconductor with a band gap width E_g equal to 3.1 eV [41]. As ceria is known to be strongly absorbing in the UV range, the DR spectrum for $\lambda < \lambda_g = 1240/E_g = 400$ nm is affected by specular reflectance. This phenomenon explains the appearance of two maxima near 350 and 275 nm for bulk ceria. The bands centred around 350 and 284 nm are assigned to Ce^{3+} and Ce^{4+} ions, respectively. The presence of a small quantity of Ce^{3+} as determined by the UV–Vis spectra is in agreement with the XPS measurements reported above. According to the literature [41–43] the band at 350 nm could be related to the presence of small crystallites which show a high surface/volume ratio. The results are in conformity with the characterization results obtained from HRTEM and XRD studies. This shift of the absorbance toward shorter wavelengths (blue shift) could then be explained by the predominance of Ce(IV)–oxygen charge transfers occurring on low coordination Ce(IV) ions.

Zirconium oxide is a direct band gap insulator showing two direct band-to-band transitions at 5.2 and 5.79 eV (238 and 214 nm, respectively) [44,45]. According to Fernandez Lopez et al. [46], eight-coordinated tetravalent Zr species (like those of cubic and tetragonal zirconias) are responsible for the absorption in the range 200–210 nm, while seven-coordinated Zr species (like those of monoclinic zirconia) are responsible for a split absorption with an additional component at 240 nm (i.e. at low energy). The bands centred around 246 and 210 nm can therefore be attributed to zirconium oxide [46,47]. According to the d^0 configuration of Zr^{4+} ions, no feature characteristics of d–d transitions are evident in the visible region (above 400 nm) in the electronic spectrum. The results are in agreement with XRD results which show the formation of a solid solution of CeO_2 and ZrO_2.

3.1.7. FT-IR

The FT-IR spectra of the catalysts are shown in Fig. 7. The broad band between 3600 and 3000 cm^{-1} with a maximum at 3404 cm^{-1} corresponds to the stretching modes of hydrogen-bonded OH groups [48]. The small peaks which appear at 2844, 2915 and 2951 cm^{-1} correspond to the υ_{C-H} region and can be attributed to the impurities of KBr, together with additional band at 1380 cm^{-1} assigned to the H–C–H symmetric bending. The band at 1611 cm^{-1} has been assigned to water (H–O–H bending). As reported in Ref. [49] the IR spectrum of pure CeO_2 displays a broad absorption with a maximum at about 360 cm^{-1} and a shoulder at 540 cm^{-1}. Agarwal et al. [50] have reported that bands for crystalline ZrO_2 appear at 435, 510 and 575 cm^{-1} for the tetragonal form and at 415, 445, 515 and 620 cm^{-1} for the monoclinic form. It is evident from the inset of Fig. 7 that a shoulder appears at 540 cm^{-1} for all three studied mixed oxides. The broad band appearing at 540 cm^{-1} is more evident for the cerium rich sample (C/Z-70/30); moreover, the peak shifts to higher wavenumbers when the zirconia content increases.

As indicated by the results reported above, the various characterization techniques give ample evidence of chemical interaction between CeO_2 and ZrO_2 resulting in a mixed oxide solid solution.

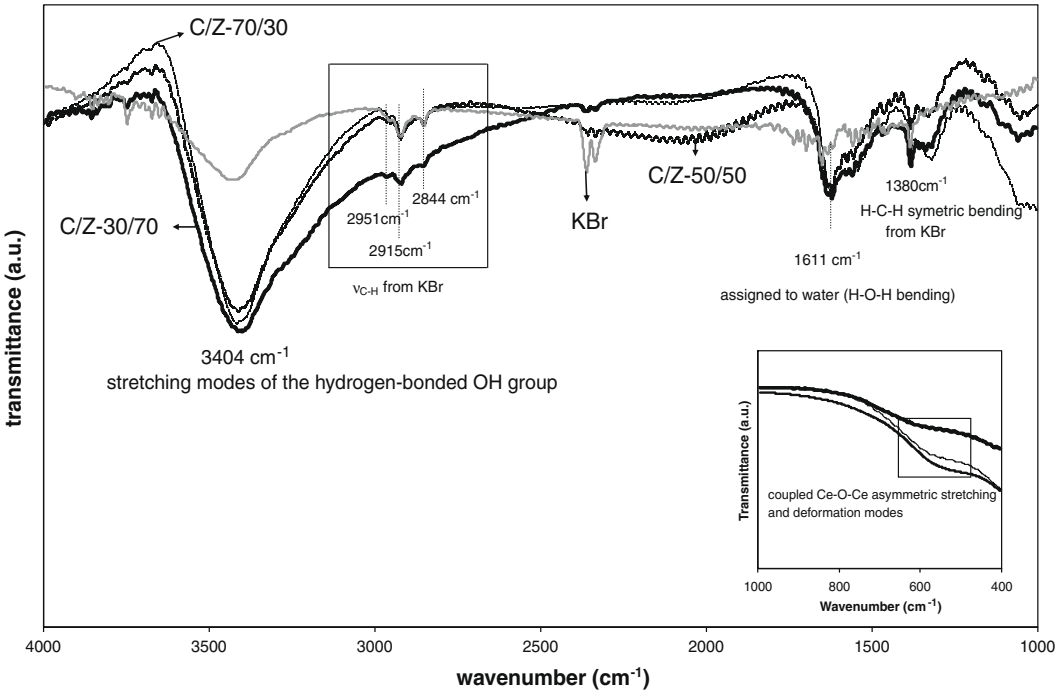

Fig. 7. Fourier transform infrared spectra of the mixed C/Z solid solutions.

3.1.8. Microcalorimetric characterization

The knowledge of the number and strength of the sites existing at the surface of a catalyst is of considerable interest, as the first step in any catalytic reaction is the adsorption and the subsequent activation of the reactant molecules on the active sites. Adsorption microcalorimetry has gained importance as one of the most reliable method for describing in detail the quantitative and energetic features of surface sites on solid catalysts. Accordingly, direct assessment of the acid–base properties of the ceria–zirconia solid solutions, in terms of both site concentrations and strength distributions, has been carried out by means of this technique, using ammonia and SO_2 as probe molecules. Information about the acidic properties of the solid solutions is summarized in Fig. 8, where the differential heats of NH_3 adsorption, Q_{diff}, have been plotted vs. ammonia uptake. The initial heats of adsorption lie in the range of 166–148 kJ/mol for the solid solutions, which is in between the adsorption heats found by Cutrufello et al. [51] for pure CeO_2 from Aldrich (76 kJ/mol) and for ZrO_2 prepared from hydrous zirconia from MEL chemicals by calcination at 700 °C (175 kJ/mol). In the region of intermediate ammonia uptake the differential heat decreases continuously for all samples, whereas in the region of high ammonia uptakes Q_{diff} falls to values characteristic of the physisorption domain (Q_{diff} < 40 kJ/mol). For all three C/Z samples the adsorption sites are continuously heterogeneous, as no plateau could be observed in the variation of differential heats with ammonia uptake.

To further compare the acid strengths of the samples, the total (n_{total}) and irreversible (n_{irr}) concentration of acidic sites have been evaluated and are presented in Table 5. It can be noted that only 30%, 25% and 20% of the total ammonia adsorbed was chemisorbed on the surface of the C/Z-30/70, C/Z-50/50 and C/Z-70/30 catalysts, respectively. Moreover, different compositions of the solid solution

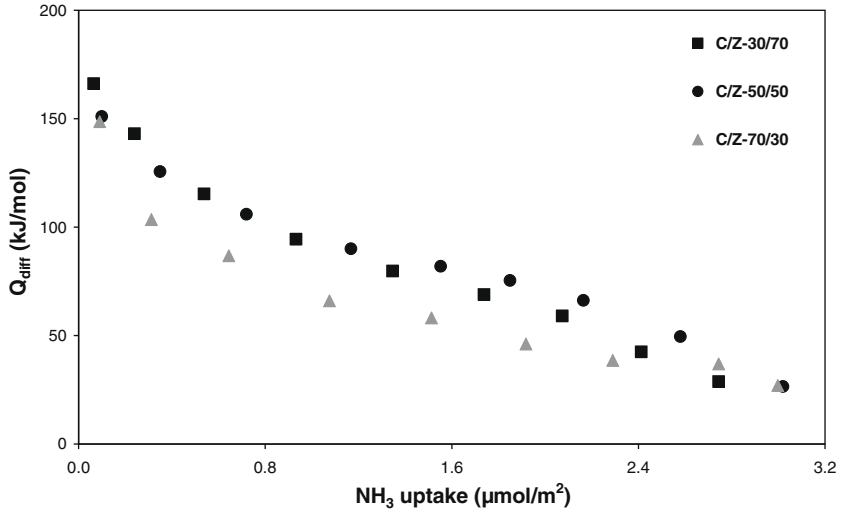

Fig. 8. Differential heats of NH_3 adsorption at 80 °C as a function of ammonia uptake (expressed in μmol/m^2 of catalyst) for the three catalysts.

Table 5
Acidity–basicity measurements of C/Z samples by microcalorimetric analysis.

Sample	NH_3		SO_2	
	n_{total}[a] (μmol/g)	n_{irr}[b] (μmol/g)	n_{total}[a] (μmol/g)	n_{irr}[b] (μmol/g)
C/Z-30/70	99.4	30.0	190.7	171.8
C/Z-50/50	75.3	18.7	130.3	115.8
C/Z-70/30	84.4	17.0	151.9	131.3

[a] Amount of NH_3 (SO_2) adsorbed at equilibrium pressure of 27 Pa.
[b] Amount of NH_3 (SO_2) irreversibly adsorbed under an equilibrium pressure of 27 Pa (amount remaining after pumping at 80 °C).

are reflected from the ammonia uptakes at high equilibrium pressures. The C/Z-30/70 exhibits the highest adsorption capacity of NH_3. It may also be interpreted that acidic sites are present more in the interior of pores, leading to more physisorption of ammonia.

The basicity of the samples has been estimated by SO_2 uptake measurements; the results obtained are presented in Fig. 9 and Table 5. The initial heats of adsorption are quite similar for all samples (190–197 kJ/mol). Significant differences could be observed when compared with NH_3 adsorption results. The SO_2 adsorption profile for the C/Z-30/70 catalyst exhibits a distinctive plateau at ca. 167 kJ/mol, characteristic of a homogeneous distribution of strong basic sites, while for the other two samples a smooth decrease is observed up to a coverage of around 2 μmol/m^2. With higher amounts a sudden drop of differential heats to values in the physisorption domain is observed for all three samples. The sudden drop may be due to monolayer formation of chemisorbed molecules on the catalyst surface. By comparing the NH_3 and SO_2 calorimetric data given in Table 5, it is revealed that all three samples possess both acidic and basic sites, with a more pronounced basic character, both in terms of concentration of basic sites and strong adsorption sites. Note also that, in contrast with the acidic character for which the adsorption sites are continuously heterogeneous, most of the adsorption sites of SO_2 form a homogeneous set of high basic strength. Reversible adsorption involves weak interactions (<50 kJ/mol) which are ascribed mainly to physisorption and are not catalytically relevant. For the determination of the relevant acidic and basic sites, the irreversibly adsorbed NH_3 and SO_2 amounts should be taken into account. The point at which the adsorption shifts from chemical, i.e. at the acidic or basic sites, to physical, must be considered in the assessment of the acidic and basic site concentrations. The physisorption is more evident when NH_3 was used as a probe molecule, which may be due to the location of acidic sites in the interior pores of the solid solutions. The strong adsorption of SO_2 is possibly due to the existence of homogeneous basic sites on the external surface of the solid solutions.

As observed from the UV–Vis and XPS spectra, Ce^{3+} is present on the catalyst surface, possibly due to the reduction of Ce^{4+} species. Another interesting observation is the existence of surface oxygen species. The maximum number of oxygen species is observed on the surface in the high zirconia content (70%) sample as shown in Table 4. It is the surface oxygen anions that act as basic sites in the calorimetric experiments. As found in the literature by NH_3-TPD analysis, the incorporation of increasing quantities of zirconia in the ceria lattice leads to a marked increase in the total and strong acidity [52]. Among the three samples, C/Z-30/70 shows distinctive features, having higher surface area, smaller particles, lower unit cell volume, more surface oxygen atoms and higher concentrations of acidic and basic sites present on the surface.

3.2. Catalyst performance in Knoevenagel condensation

The catalytic performances of ceria–zirconia solid solutions were tested in the liquid phase Knoevenagel condensation (Scheme 1) reaction using ethanol as a solvent at 80 °C, and the results are summarized in Table 6.

In the first set of experiments the Knoevenagel condensation reaction was carried out over the three different catalysts using benzaldehyde and malononitrile as substrates. The reaction was carried out under reflux conditions, until the starting materials disappeared (as checked by TLC technique). The yield was used as indicator of catalytic activity, and consequently to compare the catalytic performances of the different samples tested. As can be seen in Table 6, C/Z-30/70 was the best catalyst among the three samples in terms of reaction time and yield which varied with catalytic material. C/Z-50/50 and C/Z-70/30 samples were less active than C/Z-30/70 catalyst under similar experimental conditions, as

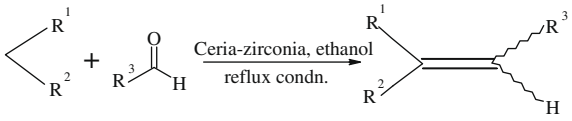

R^1, R^2 = CN, CO_2Et;

R^3 = Aryl, furoyl

Scheme 1. Knoevenagel condensation reaction.

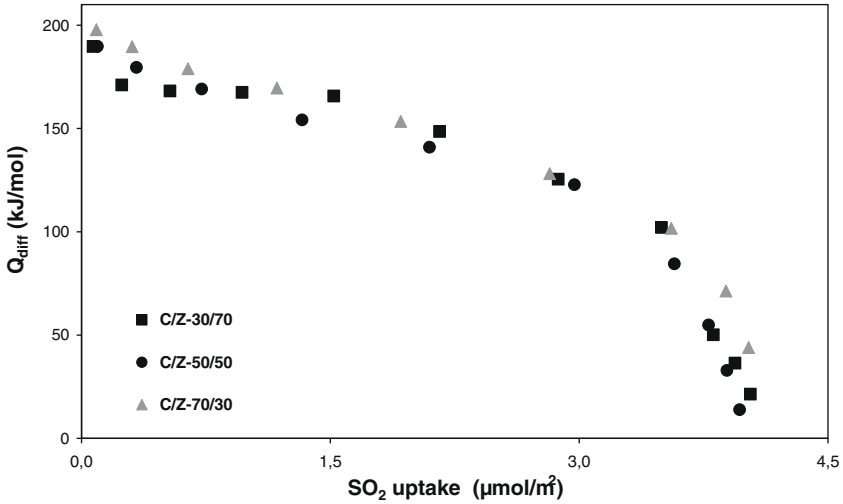

Fig. 9. Differential heats of SO_2 adsorption at 80 °C as a function of SO_2 uptake (expressed in μmol/m^2 of catalyst) for C/Z samples.

Table 6
Catalytic activity study for the three C/Z catalysts for Knoevenagel condensation.[a]

Catalyst	Yield (%)[b]	Time
C/Z-30/70	82	50 min
C/Z-50/50	57	6 h
C/Z-70/30	36	6 h

[a] *Reaction conditions:* benzaldehyde (1.0 mmol), malononitrile (1.1 mmol), catalyst 10 wt.%, ethanol medium, $T = 80$ °C. The reaction work-up was carried out as detailed under Section 2.
[b] Isolated yield after purification.

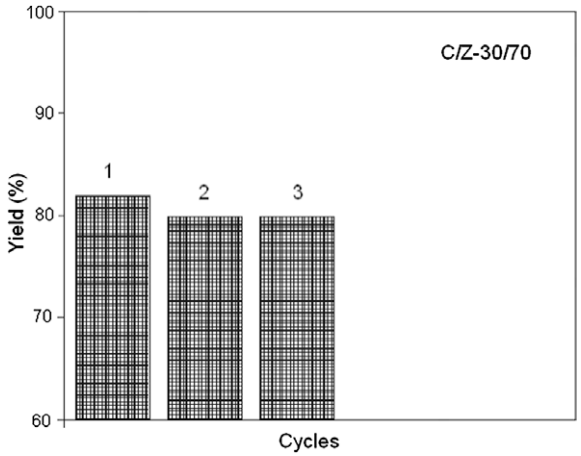

Fig. 10. Yields of benzyledene malonitrile obtained in three consecutive cycles with C/Z-30/70 catalyst in the Knoevenagel condensation reaction of benzaldehyde with malononitrile in ethanol medium at 80 °C.

evidenced from a longer duration time needed for the completion of the reaction (6 h compared to 50 min, see Table 6).

The recyclability of C/Z-30/70 sample was checked on three consecutive catalytic reaction cycles performed with benzaldehyde and malononitrile in ethanol medium at 80 °C. During each cycle, the time needed for the completion of the reaction was 50 min and the results obtained are presented in Fig. 10. The C/Z-30/70 sample exhibited consistent activity for the three cycles and thereon the catalyst slowly deactivated due to ingress of air moisture during recycling studies.

Due to its performances, C/Z-30/70 sample was then used as a catalyst for a series of reactions carried out using different types of active methylene compounds and a variety of aldehydes. The results obtained are presented in Table 7. All the products have been characterized by ^{1}H NMR, ^{13}C NMR and FT-IR spectra. Malononitrile and ethyl cyanoacetate were used as the active methylene compounds. Malononitrile was observed to be a better reagent than ethyl cyanoacetate because of its better electron-withdrawing ability. From the NMR spectroscopy it could be confirmed that the *trans* (*E*) isomer was produced exclusively.

According to the literature [53,54] two types of mechanism for the base-catalyzed Knoevenagel condensation have been found. One mechanism is the formation of imine intermediate with the base group and the other is the ion-pair mechanism. The presence of imine intermediate can be detected by *in situ* attenuated total reflection modulation spectroscopy [53]. The ion-pair mechanism involves base abstraction of a proton from the methylene carbon, forming a carbanion, which attacks the carbonyl carbon. Subsequent elimination of water results in the formation of the olefins [54]. Mild acid–base pairs in amorphous aluminophosphates and zirconophosphate oxynitrides have shown similar results, with acid–base pairs showing greater activity than solitary bases of greater strength [55].

Table 7
Knoevenagel condensation between different aldehydes and active methylene compounds using C/Z-30/70 as a catalyst.[a]

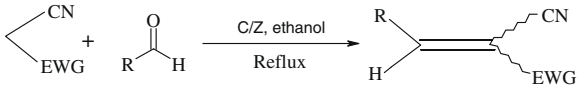

Entry	R	EWG[b]	Product[c]	Time (min)	Yield (%)[d]
1	C_6H_5	CN	**2a**	50	82
2	C_6H_5	CO_2Et	**2b**	75	78
3	4-NO_2–C_6H_4	CN	**2c**	45	90
4	4-NO_2–C_6H_4	CO_2Et	**2d**	55	85
5	4-CH_3–C_6H_4	CN	**2e**	60	78
6	4-CH_3–C_6H_4	CO_2Et	**2f**	90	72
7	4-Cl–C_6H_4	CN	**2g**	60	81
8	4-Cl–C_6H_4	CO_2Et	**2h**	60	78
9	2-NO_2–C_6H_4	CN	**2i**	45	85
10	3-NO_2–C_6H_4	CO_2Et	**2j**	45	83
11	Furoyl	CN	**2k**	60	83
12	Furoyl	CO_2Et	**2l**	90	81

[a] *Reaction conditions:* aldehyde (1.0 mmol), active methylene compound (1.1 mmol), catalyst 10 wt.%, ethanol medium, $T = 80$ °C. The reaction work-up was carried out as detailed under Section 2.
[b] Electron-withdrawing group.
[c] All products are known compounds and their spectra (NMR and IR) are in accordance with literature values; only *E* isomer was formed as confirmed from NMR spectroscopy.
[d] Isolated yield after purification.

In the present case the acidic sites, present in the pores, are responsible for coordinating with nitrile groups, thereby facilitating abstraction of the ethyl cyanoacetate proton by basic sites. Though the basic properties of the samples are expected to determine their catalytic behavior, no evident correlation could be found between the catalytic performances of the samples and their basic character alone (the yield decreased in the order C/Z-30/70 > C/Z-50/50 > C/Z-70/30, while the basic character decreased in the order C/Z-30/70 > C/Z-70/30 > C/Z-50/50). But it is important to note that there is a close relation between the yield values and the number of strong acidic sites (see n_{irr} (NH_3) in Table 5), both increasing from C/Z-70/30 to C/Z-30/70. It seems that the coordination on acidic sites of the nitrile group depends on the relative strength of the former and it is an important step in controlling the rate of the condensation reaction. As measured in the calorimetric study, the C/Z-30/70 had the highest concentration of strong acidic and basic sites and therefore showed the best catalytic activity. It can be concluded, regarding the results obtained, that the concentration of strong acidic sites is an important parameter in this reaction. The ratio of the number of strong basic to acidic sites (n_{irr} (SO_2)/n_{irr} (NH_3)) has been calculated for each catalyst from the microcalorimetry results, by dividing the amount of irreversibly adsorbed SO_2 by the amount of irreversibly adsorbed NH_3. The values obtained for this parameter are 5.72, 6.19 and 7.74 for C/Z-30/70, C/Z-50/50 and C/Z-70/30, respectively. As can be observed, the lower this parameter is, the higher the yield of the Knoevenagel condensation product is. Therefore, it can be concluded that promising results can be obtained using a bifunctional acid–base catalyst when both functions are well balanced and that an optimal ratio of basic to acidic sites has to be reached to get the best catalytic performances.

4. Conclusions

In this study, $Ce_xZr_{1-x}O_2$ nanocrystalline solid solutions have been prepared, characterized and used as efficient and stereoselective catalysts for Knoevenagel condensation in a pathway that does

not involve any hazardous chemicals, keeping the process environmentally friendly.

The direct correlation between the concentration of acidic sites and the yield of the products indicated that a higher concentration of acidic sites gives more products in the reaction even if the presence of basic sites remains obligatory. Indeed, the ratio of basic to acidic sites (n_{irr} (SO_2)/n_{irr} (NH_3)) was found to influence the product formation: the lower this ratio is, the higher the product yield is. Thus, the present data illustrate that designing bifunctional acid–base catalyst with an optimal ratio of basic to acidic sites constitutes an effective and viable tool for increasing the catalytic activity.

$Ce_xZr_{1-x}O_2$ catalysts can be interesting alternatives to soluble bases in view of the following advantages: (a) high catalytic activity under mild reaction conditions; (b) easy separation of the catalyst after the reaction and (c) reusability of the catalyst.

Acknowledgments

One of the authors (B.C.) would like to acknowledge DST, Govt. of India for funding under Fast Track Young Scientist Scheme (Proposal Number SR/FTP/ETA-16/2007), New Delhi, for providing financial assistance.

Dr. François Figueras from IRCELYON is gratefully acknowledged for fruitful discussions.

The authors are thankful to the scientific services of IRCELYON.

References

[1] M. Epifani, E. Pellicer, J. Arbiol, J.R. Morante, Chem. Mater. 21 (2009) 862.
[2] X. Liu, K. Zhou, L. Wang, B. Wang, Y. Li, J. Am. Chem. Soc. 131 (2009) 3140.
[3] A. Trovarelli, Catal. Rev. – Sci. Eng. 38 (1996) 439.
[4] M. Pijolat, M. Prin, M. Soustelle, O. Tourette, J. Chem. Phys. 91 (1994) 37.
[5] C.S. Wright, R.I. Walton, D. Thompsett, J. Fisher, Inorg. Chem. 43 (2004) 2189.
[6] C.S. Wright, J. Fisher, D. Thompsett, R.I. Walton, Angew. Chem. Int. Ed. 45 (2006) 2442.
[7] X. Liang, X. Wang, Y. Zhuang, B. Xu, S. Kuang, Y. Li, J. Am. Chem. Soc. 130 (2008) 2736.
[8] M. Alifanti, B. Baps, N. Blangenois, J. Naud, P. Grange, B. Delmon, Chem. Mater. 15 (2003) 395.
[9] N. Hosseinpour, A.A. Khodadadi, Y. Mortazavi, A. Bazyari, Appl. Catal. A: Gen. 353 (2009) 271.
[10] P. Fornasiero, R. Di Monte, G.R. Rao, J. Kašpar, S. Meriani, A. Trovarelli, M. Graziani, J. Catal. 151 (1995) 168.
[11] B.M. Reddy, B. Chowdhury, P.G. Smirniotis, Appl. Catal. A: Gen. 211 (2001) 19.
[12] J.R. Kim, W.J. Myeong, S.K. Ihm, J. Catal. 263 (2009) 123.
[13] V. Solinas, E. Rombi, I. Ferino, M.G. Cutrufello, G. Colón, J.A. Navio, J. Mol. Catal. A: Chem. 204–205 (2003) 629.
[14] L. Liu, Y. Chen, L. Dong, J. Zhu, H. Wan, B. Liu, B. Zhao, H. Zhu, K. Sun, L. Dong, Y. Chen, Appl. Catal. B: Environ. 90 (2009) 105.
[15] B.M. Reddy, G. Thrimurthulu, P. Saikia, P. Bharali, J. Mol. Catal. A: Chem. 275 (2007) 167.
[16] F. Freeman, Chem. Rev. 80 (1980) 329.
[17] G. Jones, Knoevenagel Condensation in Organic Reaction, vol. 15, Wiley, New York, 1967, p. 204.
[18] L.F. Tietze, Chem. Rev. 96 (1996) 115.
[19] M.D. Gracia, M.J. Jurado, R. Luque, J.M. Campelo, D. Luna, J.M. Marinas, A.A. Romero, Micropor. Mesopor. Mater. 118 (2009) 87.
[20] Sujandi, E.A. Prasetyanto, S.E. Park, Appl. Catal. A: Gen. 350 (2008) 244.
[21] Y. Goa, P. Wu, T. Tatsumi, J. Catal. 224 (2004) 107.
[22] F. Santamarta, P. Verdia, E. Tojo, Catal. Commun. 9 (2008) 1779.
[23] J.D. Bass, S.L. Anderson, A. Katz, Angew. Chem. Int. Ed. 42 (2003) 5219.
[24] A. Katz, M.E. Davis, Nature 403 (2000) 286.
[25] S.L. Hruby, B.H. Shanks, J. Catal. 263 (2009) 181.
[26] G. Bergeret, P. Gallezot, in: G. Ertl, H. Knozinger, F. Schuth, J. Weitkamp (Eds.), Particle Size and Dispersion Measurements in Handbook of Heterogeneous Catalysis, vol. 2, Wiley-VCH, Verlag, 2008, p. 738.
[27] D.G. Lamas, R.O. Fuentes, I.O. Fábregas, M.E. Fernández de Rapp, G.E. Lascalea, J.R. Casanova, N.E. Walsöe de Reca, A.F. Craievich, J. Appl. Crystallogr. 38 (2005) 867.
[28] A. Auroux, Top. Catal. 19 (2002) 205.
[29] P.B. Weisz, J.S. Hicks, Chem. Eng. Sci. 17 (1962) 265. and the references therein.
[30] A.I. Vogel, in: B.S. Furniss, A.J. Hannaford, P.W.G. Smith, A.R. Tatchell (Eds.), Textbook of Practical Organic Chemistry, fifth ed., Longman Science & Technical, New York, 1988, p. 199.
[31] G. Colon, M. Pijolat, F. Valdivieso, H. Vidal, J. Kaspar, E. Finocchio, M. Daturi, C. Binet, J.C. Lavalley, R.T. Baker, S. Bernal, J. Chem. Soc., Faraday Trans. 94 (1998) 3717.
[32] (a) S. Meriani, Mater. Sci. Eng. 71 (1985) 369;
(b) S. Meriani, Mater. Sci. Eng. A 109 (1989) 121.
[33] B.M. Reddy, A. Khan, Y. Yamada, T. Kobayashi, S. Loridant, J.C. Volta, J. Phys. Chem. B 107 (2003) 11475.
[34] M. Teng, L. Luo, X. Yang, Micropor. Mesopor. Mater. 119 (2009) 158.
[35] A. Muto, T. Bhaskar, Y. Kaneshiro, Y. Sakata, Y. Kusano, K. Murakami, Appl. Catal. A: Gen. 275 (2004) 173.
[36] M. Adamowska, S. Muller, P. Da Costa, A. Krzton, P. Burg, Appl. Catal. B: Environ. 74 (2007) 278.
[37] T. Yuzhakova, V. Rakic, C. Guimon, A. Auroux, Chem. Mater. 19 (2007) 2970.
[38] K.I. Seo, P.C. Mclntyre, H. Kim, K.C. Saraswat, Appl. Phys. Lett. 86 (2005) 082904.
[39] A. Dittmar, D.L. Hoaug, A. Martin, Thermochim. Acta 470 (2008) 40.
[40] X. Liang, X. Wang, Y. Zhuang, B. Xu, S. Kuang, Y. Li, J. Am. Chem. Soc. 130 (2008) 2736.
[41] G. Balducci, J. Kaspar, P. Fornasiero, M. Graziani, M. Saiful Islam, J. Phys. Chem. B 102 (1998) 557.
[42] A. Bensalem, F. Bozon-Verduraz, M. Delamar, G. Bugli, Appl. Catal. A: Gen. 121 (1995) 81.
[43] S. Damyanova, C.A. Perez, M. Schmal, J.M.C. Bueno, Appl. Catal. A: Gen. 234 (2002) 271.
[44] H. Ranjan Sahu, G. Ranga Rao, Bull. Mater. Sci. 23 (2000) 349.
[45] A. Emeline, G.V. Cataeva, A.S. Litke, A.V. Rudakova, V.K. Ryabchuk, N. Serpone, Langmuir 14 (1998) 5011.
[46] E. Fernandez Lopez, V. Sanchez Escribano, M. Panizza, M.M. Carnasciali, G. Busca, J. Mater. Chem. 11 (2001) 1891.
[47] A. Pepe, M. Aparicia, S. Ceré, A. Duran, J. Non-Cryst. Solids 348 (2004) 162.
[48] V. Sanchez Escribano, E. Fernandez Lopez, M. Panizza, C. Resini, J.M. Gallardo Amores, G. Busca, Solid State Sci. 5 (2003) 1369.
[49] V. Sanchez Escribano, E. Fernandez Lopes, J.M. Gallardo-Amores, C. del Hoyo Martinez, C. Pistarino, M. Pauizza, C. Resini, C. Busca, Combust. Flame 153 (2008) 97.
[50] M. Agarwal, M.R. De Guire, A.H. Heuer, J. Am. Ceram. Soc. 80 (1997) 2967.
[51] M.G. Cutrufello, I. Ferino, V. Solinas, A. Primavera, A. Trovarelli, A. Auroux, C. Picciau, Phys. Chem. Chem. Phys. 1 (1999) 3369.
[52] B. De Rivas, R. Lopez-Fonseca, J.R. Gonzalez Velasco, J.J. Gutirrez-Orlitz, Catal. Commun. 9 (2008) 2018.
[53] R. Wirz, D. Ferri, A. Baiker, Langmuir 22 (2006) 3698.
[54] A. Corma, V. Fornes, R.M. Martin Aranda, H. Garcia, J. Primo, Appl. Catal. 59 (1990) 237.
[55] M.J. Climent, A. Corma, S. Iborra, A. Velty, J. Mol. Catal. A: Chem. 182–183 (2002) 327.